

## Investigation of symmetric non-spherical particle shapes by applying low-resolution spherical harmonics

Urtė Radvilaitė, Rimantas Kačianauskas, Dainius Rusakevičius

Department of Strength of Materials and Engineering Mechanics,  
Vilnius Gediminas Technical University,  
Saulėtekio ave. 11, LT-10223 Vilnius, Lithuania  
[urte.radvilaite@vgtu.lt](mailto:urte.radvilaite@vgtu.lt)

**Received:** April 17, 2016 / **Revised:** July 19, 2016 / **Published online:** December 2, 2016

**Abstract.** The issue of mathematical modelling of non-spherical shapes of particles is considered. Thus, application of the spherical harmonics (SH) technique in modelling the simplest symmetric star-shaped particles is demonstrated by applying low-resolution functions. The investigation was restricted to a circular cylinder and a rectangular parallelepiped, geometrically primitive, but widespread oblate industrial shapes. The modelling quality was studied by considering selected error norms and the most important integral characteristics of a particle geometry, including the surface area and volume. The presented results discovered new features of the spherical harmonic technique and enhanced understanding of their applicability to describe non-spherical shapes.

**Keywords:** low-resolution spherical harmonics, symmetric star-shaped particles, circular cylinder, rectangular parallelepiped.

### 1 Introduction

Mathematical modelling and information technologies play an important role in many areas of sciences and engineering. Among many specific applications, particulate solids, especially granular materials, could be distinguished. They present a huge class of materials widely used in chemical, pharmaceutical, food and other industries.

An important property of particulate solid is the shape of particle. The research addressing the characterisation and mathematical description of a particle shape concerns basically non-spherical shapes. Recently, many different mathematical models, that constitute particle shapes, have been systematically formulated and utilized by applying computational and information technologies.

One of semi-analytical methods, spherical harmonic functions (SH), have gained much interest due to their contribution in many fields. The three-dimensional mathematical analysis of particle shape, using spherical harmonics with application to aggregates used in concrete, was started by Garboczi [9]. Here, mathematical aspects of spherical harmonic series were also provided. The investigation of SH, especially in combination

with the available imaging technique, was continued in a series of works by Garboczi and his co-workers. The method was successfully applied in the description of sand [15] or even to quite specific lunar regolith particles [10]. SH principally works with star-shaped particles and various shape indicators were considered in [3, 11]. Contribution of other authors could also be pointed out [7, 18].

Computational models of granular solids are developed within the framework of the discrete element method (DEM). DEM presents the Lagrangian type modelling technique pioneered by [5] that offers a direct way of investigating solution by tracing the motion of individual particles numerically, i.e. by computing positions, angular rotations, velocities, forces, and all other estimates in time. It has been defined that the behaviour of particles during motion and inter-particle contacts mostly depend on their shapes. The standard DEM framework was elaborated on the basis of a spherical particle. Critical reviews of recent developments in DEM with advances in the formulation and implementation of particle shape models are given in [6, 14, 16]. The recent study is aimed to demonstrate the basic features of spherical harmonic modelling methodology, addressing the applicability of low-resolution spherical harmonics to describe a symmetric particle shape, limited by the expansion degree  $L = 3$ .

The paper is organised as follows. A unified modelling methodology and data structure, demonstrating the hierarchy of models, is developed and described in Section 2. A detailed SH analysis of two very popular representative shapes of industrial particles with sharp edges, i.e. circular cylinder and rectangular parallelepiped, is presented in Sections 3 and 4, respectively. The comparison of the study of selected shapes of varying flatness is shown in detail in Section 5, while conclusions are drawn in Section 6.

## 2 Methodology of spherical harmonics

### 2.1 A modelling concept

A particle is assumed to be a continuous star-shaped 3D body obeying the symmetry, where at least one symmetry plane exists. It is described in the local frame of reference, while two local coordinate systems – Cartesian coordinates  $Oxyz$  or spherical coordinates  $Or\varphi\theta$  with their origin positioned in the centre of mass – can be simultaneously applied to describe the particle. When applying spherical coordinates, the position of a point is defined by the polar radius  $r$  and two polar and azimuthal spherical angles,  $\varphi$  and  $\theta$ , varying within the limits  $0 \leq \varphi \leq 2\pi$  and  $0 \leq \theta \leq \pi$ , respectively. The coordinate frame and positioning of point  $p$ , defined by the Cartesian coordinates  $\mathbf{x}_p$  and spherical coordinates  $r_p$ ,  $\varphi_p$  and  $\theta_p$ , are shown in Fig. 1.

The direct relationship allows a parametric evaluation of Cartesian coordinates

$$x = r \cos \varphi \sin \theta, \quad y = r \sin \varphi \sin \theta, \quad z = r \cos \theta. \quad (1)$$

An inverse relationship to spherical coordinates

$$r = (x^2 + y^2 + z^2)^{1/2}, \quad \varphi = \tan^{-1} \frac{y}{x}, \quad \theta = \cos^{-1} \frac{z}{r} \quad (2)$$

could also be used.

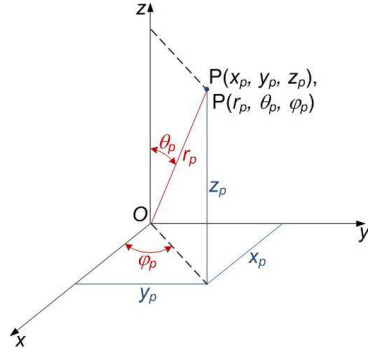


Figure 1. Coordinate frame and positioning of the point  $p$ .

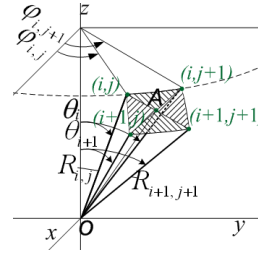


Figure 2. Scheme for the numerical integration.

The modelling concept elaborated and applied hereafter operates systematically with the specified surfaces manifested in terms of three categories, namely, original, reference, and actual. These different categories are characterised by different mathematical models, and they are considered at different modelling stages. The *original* model, denoted hereafter by  $S$ , presents a surface that exactly matches the particle shape. Explicitly, the original surface in Cartesian coordinates is described as follows:

$$S(\mathbf{x}) = 0. \tag{3}$$

Referring to spherical coordinates, the original surface is described by the polar radius  $r$ , varying as a function of the polar angles  $\varphi$  and  $\theta$ :

$$r(\varphi, \theta) = S_R(\varphi, \theta). \tag{4}$$

Another definition of the surface is referred to as the *reference* surface, denoted hereafter by  $R$ , which is assumed to be a discrete model of the original surface  $S$ . Since the reference surface is only an approximated surface, it is not unique. The definition of the reference surface assumes the existence of the family of  $k$  reference surfaces  $R_k$ , each of which is denoted by subscript  $k$ , where  $k = 1, 2, \dots, K$ . The reference surface  $R_k$  is specified as a discrete set  $\mathbf{x}_k = \{\mathbf{x}_{k1}, \dots, \mathbf{x}_{kp}, \dots\}$  consisting of the coordinates  $\mathbf{x}_{kp}$  of  $p = 1, 2, \dots, N_k$  sampling points.

On the other hand, the reference surface can be formed by applying various modelling strategies, denoting each particular strategy by a subscript  $q$  ( $q = 1, 2, 3, \dots$ ). As a result, a double indexing of reference surfaces is applied, and each of them is denoted as  $R_{qk}$ , but defined by the vector  $\mathbf{x}_{qk}$ .

Alternatively, the reference surface  $R_{qk}$  can be considered in spherical coordinates and defined by the discrete values of the polar radius  $\mathbf{r}_{qk} = \{r_{qk1}, \dots, r_{qkp}, \dots\}$ . Using Eq. (4), the reference surface  $R_{qk}$  can be related to discrete sets of spherical angles  $\varphi_{qk}$  and  $\theta_{qk}$ , characterising sampling points as follows:

$$\mathbf{r}_{qk}(\varphi_{qk}, \theta_{qk}) = \mathbf{S}_R(\varphi_{qk}, \theta_{qk}). \tag{5}$$

The *actual* surface, denoted hereafter by  $A$ , presents a semi-analytical approximation of the original surfaces  $S$ , restricting to the description in spherical coordinates  $A(\varphi, \theta) \approx S_R(\varphi, \theta)$ , where the actual model  $A$  is presented by a truncated series, containing the finite number  $M$  of terms. Here, each term  $a_i f_i(\varphi, \theta)$  is the product of unknown coefficients  $a_i$  and analytically specified polynomials  $f_i(\varphi, \theta)$ , where  $i = 1, 2, \dots, M$ . The scalar product can be presented in the vector form:

$$A(\varphi, \theta) = \mathbf{f}(\varphi, \theta)^T \cdot \mathbf{a}. \quad (6)$$

Here, unknown coefficients form a vector  $\mathbf{a} = \{a_1, \dots, a_2, \dots, a_M\}^T$ , while polynomials  $\mathbf{f}(\varphi, \theta)$  are formed in the same manner. The complexity level of the approximation in Eq. (6) is defined by the number  $M_j$  of polynomials. Fixing hierarchically different values of  $M_j$ , different actual models  $A_j(\varphi, \theta)$  with the different complexity, defined by the subscript  $j$  ( $j = 1, \dots, L$ ), may be developed.

Each of the hierarchically developed actual surfaces  $A_j$  describes the original surface  $S$  on the basis of the discretely defined reference surfaces  $R_{qk}$ . In summary, each of the actual surfaces  $A_{jqk}(\varphi, \theta) \equiv A_{jqk}(\mathbf{a}_{jqk}, \mathbf{f}_j(\varphi_{qk}, \theta_{qk}))$ , apart from their complexity level  $j$ , involves the properties of reference model  $R_{qk}$  reflecting the modelling strategy  $q$  and the sampling model  $k$ . The evaluation procedure is implemented, however, by approximating the reference surfaces  $R_{qk}$ .

## 2.2 Spherical harmonics expansion

To develop a modelling technique and to characterize the actual surface of a particle, the spherical harmonics expansion will be considered. A formal approach to spherical harmonics may be easily found in purely mathematical [17] or specific particle shape-oriented applications [7,9]. Spherical harmonics are complex functions, but only the real-valued terms, obtained by separating imaginary and real parts, are used in this application. Applying them, the actual surface defined by Eq. (6) is transformed to the SH expression

$$A(\varphi, \theta) \cong \sum_{l=0}^L \sum_{m=-l}^l a_l^m Y_l^m(\varphi, \theta). \quad (7)$$

The maximal order of the spherical harmonic expansion is usually defined by an integer parameter called the expansion degree  $L$ . Consequently, each expansion term  $a_l^m$  and  $Y_l^m(\varphi, \theta)$  is characterised by two indices. The subscript  $l$  ( $l = 0, 1, 2, \dots, L$ ) indicates the expansion degree, while the superscript  $m$  ( $m = -l, \dots, 0, \dots, l$ ) indicates the order of spherical harmonics.

It is obvious that the expansion degree  $L$  predefines the number of actual models  $j$  ( $j = 1, 2, \dots, L$ ), while the total number of terms is defined as

$$M = \sum_{l=0}^L (2l + 1) = (L + 1)^2. \quad (8)$$

The expressions of spherical harmonics expansion are adapted to plane symmetric shapes of the body. Consequently, the original harmonics were characterized by their

moduli and were described by the expressions adjusted as follows:

$$Y_l^m(\varphi, \theta) = \begin{cases} \sqrt{2}C_l^m |\cos(m\varphi)P_l^m(\cos\theta)| & \text{if } m > 0, \\ C_l^0 |P_l^0(\cos\theta)| & \text{if } m = 0, \\ \sqrt{2}C_l^{|m|} |\sin(|m|\theta)P_l^{|m|}(\cos\varphi)| & \text{if } m < 0, \end{cases} \quad (9)$$

where the expression  $P_l^m(\cos\theta)$  stands for associated Legendre polynomials [9],  $C_l^m$  is a normalization constant given by

$$C_l^m = \sqrt{\frac{2l+1}{4\pi} \frac{(l-m)!}{(l+m)!}}. \quad (10)$$

The hierarchical structure of spherical harmonics specified by double indices  $l$  and  $m$ , used in Eq. (7), should be utilised in Eq. (6) with respect to Eqs. (8)–(10).

### 2.3 Low-resolution harmonics

Application of spherical harmonics was basically focussed on capturing complex shapes [7, 10, 12, 18], where the significance of higher resolution harmonics was emphasised. It is noteworthy that the accuracy of a semi-analytical approximation model is controlled by a suitable value of expansion degree  $L$  of spherical harmonics that depends on particle shape. We shall examine the capabilities of the method looking for the performance of low-resolution harmonics as a potential candidate for DEM applications. Several advantages related to the low-resolution harmonics are expected. They comprise relative simplicity of the expression, limited with the finite number of terms, but also the unification of modelling approach applicable to different shapes. To increase the approximation accuracy of low-resolution harmonics, adaptive shape-related strategies will be examined.

To meet the simplicity requirements, we limit our investigation to the highest expansion degree  $L = 3$ , defined by  $M = 16$  coefficients. Now, the structure of expression Eq. (6) is illustrated by the sample with  $L = 3$  elaborating  $i$  ( $i = 1, \dots, 16$ ) terms. The vector of coefficients  $\mathbf{a} = \{a_1, a_2, \dots, a_i, \dots, a_{16}\}^T$ , relevant to spherical harmonics, is defined according to Eq. (7). It illustrates a double indexing system and has the following structure:  $\mathbf{a} = \{a_0^0, a_1^{-1}, a_1^0, a_1^1, a_2^{-2}, a_2^{-1}, a_2^0, a_2^1, a_2^2, a_3^{-3}, a_3^{-2}, a_3^{-1}, a_3^0, a_3^1, a_3^2, a_3^3\}^T$ , while the polynomials  $f_i \equiv Y_l^m$  are formed by harmonic functions in the same manner. The explicit expressions are presented in Table A.1 in Appendix.

### 2.4 Calculation of harmonic coefficients

The evaluation of polynomial coefficients Eq. (6) can be considered by exploring a linear relationship between the reference and actual surfaces. Regarding expression (7) with respect to Eqs. (8)–(10), Eq. (5) may be written as a linear matrix equation. Considering an arbitrarily specified reference model  $R_{qk}$ , defined by fixed values of the sampling points  $\varphi_{qk}$  and  $\theta_{qk}$ , a linear equation reads as follows:

$$[\mathbf{Y}_j(\varphi_{qk}, \theta_{qk})] \mathbf{a}_{jqk} = \mathbf{r}_{qk}(\varphi_{qk}, \theta_{qk}). \quad (11)$$

Here,  $[\mathbf{Y}_j]$  stands for a rectangular transformation matrix, relating unknown coefficients  $\mathbf{a}_{jqk}$  with the discrete values  $\mathbf{r}_{qk}(\varphi_{qk}, \theta_{qk})$  of the original surface  $S_R$ , defined at the sampling points of the reference model.

The number of columns  $M$  of the transformation matrix is predefined by the expansion degree  $L$ , obtained according to Eq. (8). The number of rows  $N$  is equal to the number of sampling points. In general, the number of sampling surface points  $N > M$  is large enough to meet the required precision. Generation of this matrix is rather a routine task, because each column  $i$  of the matrix, corresponding to the specified harmonic term, is filled with the values of harmonic functions  $Y_l^m$  for the whole range of sampling points. This evaluation technique has been recently demonstrated in [18].

Mathematical aspects of the approximation problem in Eq. (11) and solution properties are discussed in [4]. Using the matrix algebra, a solution is obtained by a rather standard pseudo-inversion procedure

$$\mathbf{a}_{jqk} = [\mathbf{Y}_{jqk}]^+ S_{R,qk}(\varphi_{qk}, \theta_{qk}). \quad (12)$$

Here, a pseudo-inverse matrix is formally defined by the expression

$$[\mathbf{Y}_{jqk}]^+ = [\mathbf{Y}_{jqk}]^T ([\mathbf{Y}_{jqk}][\mathbf{Y}_{jqk}]^T)^{-1}. \quad (13)$$

Whenever the rank is lower, the solution of the above problem is non-unique. Consequently, Eq. (11) yields a non-unique set of coefficients. In this case, the generalised Moore–Penrose pseudo-inversion approach is applied further in the evaluation of a unique set of coefficients.

It could be mathematically shown (see [4]), that the pseudo-inversion in Eq. (12) is equivalent to the least-squares approximation. The quality of approximation could be estimated by the least-squares error norm.

## 2.5 Descriptors of a particle shape

Various particle parameters and descriptors can be used for characterizing a particle shape. Deviation of the actual surface from the original shape is a natural descriptor. When applying spherical coordinates, such a descriptor  $D(\varphi, \theta)$  is identified with a continuous error between the original and actual surface.

The main weakness of the arbitrarily discrete error descriptor is that it minimises errors at sampling points, while the in-between error is not controlled. For increasing robustness of descriptors, a reference threshold model, denoted hereafter by the abbreviation *thr*, is introduced. It is defined by a dense grid, the number of sampling points  $N_{\text{thr}}$  of which is substantially larger as compared to that of reference models used for approximation purposes, and locations of these points are different. As a result, deviation of the actual surface from the original one, described in Eq. (11), is estimated by deviations at each point  $p$  from the reference threshold. An arbitrarily actual surface is characterised by a discrete descriptor, calculated with respect to the reference threshold

$$\mathbf{D}_{jqk}(\varphi_{\text{thr}}, \theta_{\text{thr}}) = [\mathbf{Y}_j(\varphi_{\text{thr}}, \theta_{\text{thr}})] \mathbf{a}_{jqk} - \mathbf{r}_{qk}(\varphi_{\text{thr}}, \theta_{\text{thr}}). \quad (14)$$

Characterisation of the actual model, obtained using a specified discrete set, is performed further in terms of Euclidean and maximal error norms. The Euclidean norm

$$\|\mathbf{D}_{jqk}\|_2 = \left( \sum_{p=1}^{N_{\text{thr}}} \mathbf{D}_{jqk}(\varphi_p, \theta_p)^2 \right)^{1/2} \quad (15)$$

is applied in evaluating the suitability of the model over the entire domain. A more sophisticated normalized least-squares error norm of surface weighting was used in [7]. The maximum error norm

$$\|\mathbf{D}_{jqk}\|_\infty = \max_{p=1, N_{qk}} \mathbf{D}_{jqk}(\varphi_p, \theta_p). \quad (16)$$

characterises the local deviations.

Another category of descriptors, the surface area  $A$  and the volume of particle  $V$ , are the most often applied integral quantities. Theoretically, the surface area of the particle is considered in spherical coordinates by integrating the surface over the entire angular subdomain. Numerical integration procedure was utilised on the basis of the reference model, where cells are formed by a polar grid (Fig. 2). Splitting a cell into a patch of four triangles, the discrete surface is composed of triangles.

Geometry of a triangle is defined by three vectors of three vertices, the point coordinates of which are given by the vectors  $\mathbf{x}_1 = \{x_1, y_1, z_1\}^T$ ,  $\mathbf{x}_2 = \{x_2, y_2, z_2\}^T$ , and  $\mathbf{x}_3 = \{x_3, y_3, z_3\}^T$ . The area of this triangle embedded in a three-dimensional Cartesian space is expressed as a modulus of the vector product

$$A_{\text{tr}} = \frac{1}{2} \|(\mathbf{x}_3 - \mathbf{x}_1) \times (\mathbf{x}_2 - \mathbf{x}_1)\|. \quad (17)$$

Calculation of the volume follows the same path. Since the triangles are already formed, calculation of the entire volume for the whole body is equal to the sum of all volumes of pyramids. Applying vector algebra, the volume of a pyramid is calculated as a mixed triple product of coordinate vectors of the surface triangle

$$V_{\text{pyr}} = \frac{1}{3} \mathbf{x}_1 \cdot (\mathbf{x}_2 \times \mathbf{x}_3). \quad (18)$$

## 2.6 Modelling strategies for specified shapes

In practical situations, the accuracy of a specified shape described by spherical harmonics depends not only on the complexity of expansion, but also, even more, on the suitability of the reference model. The issue on formation of the reference surface  $R_{qk}$  involves two steps: 2D positioning of sampling points, defined by the vectors  $\varphi_{qk}$  and  $\theta_{qk}$  in the  $\varphi\theta$ -subspace, and calculation of surface points in the three-dimensional space  $\mathbf{r}_{qk}(\theta_{qk}, \varphi_{qk})$  applying Eq. (4). The choice of a reference model may be considered as mathematical parameterization of a mesh representing the surface.

The problem, however, is not strictly mathematical, while the practical implementation of positioning comprises heuristic arguments formulated in terms of an appropriate

modelling strategy. Each of the strategies conditionally denoted by a subscript  $q$  stands for a heuristic rule how to construct a grid by generating different sets  $k$  ( $k = 1, 2, \dots, K$ ) of sampling points  $\varphi_{qk}$  and  $\theta_{qk}$ . Each new set of points  $k + 1$  is obtained on the basis of the previous set  $k$ .

For practical implementation of the positioning, several strategies aimed to specify low-resolution harmonics are elaborated and tested numerically. Each of the strategies is based on specified assumptions. The grid-based strategies employ a concept of grid that covers a modelling sub-domain dividing it into cells, while the sampling points are embedded into nodes of the grid. By applying the sequential refinement strategy, a finer grid is formed by a regular sub-division of grid cells. The strategy offers a relatively simple method, however, the discussion presented in [17] points out the difficulties to predict the size of a cell that satisfies the given tolerance.

An adaptive refinement strategy forms an irregularly shaped family of grids, where the size of cells varies according to the specified rules. The character of surface should be taken into account, and the size of grid cells is adapted to match the variation of the surface.

The Gaussian point strategy is applied to generate a surface using the Gaussian integration points as sampling points. In general, the Gaussian points present a part of the numerical Gaussian quadrature integration method. The practical application of this technique in the particle shape analysis is reported by Garboczi [9], however, it is limited to a relatively high order quadrature with a large number up to 120 points. The efficiency of this technique meant for low harmonics is of our interest.

### 3 SH modelling of a circular cylinder

#### 3.1 Modelling approach

Historically, DEM started with the most suitable shape, i.e. a perfect sphere. Recently, a circular cylinder and a rectangular parallelepiped (Fig. 3) are frequently used for modelling of particles. The circular cylinder (Fig. 3a), is classified to a specific category of particle shapes used in DEM [13].

The cylinder refers to the Cartesian coordinates, where the central axis of the cylinder coincides with the Cartesian axis  $Oz$ . The cylinder body is limited by cylinder surface and two perpendicular cut-planes  $z = \pm c$ . In Cartesian coordinates, the cylinder surface is described by the continuous non-smooth function  $S_{\text{cyl}}(\mathbf{x})$  described by Eq. (C1). The surface has a sharp circular edge in the section of surface with planes. Alternatively, the cylinder surface  $S_{R,\text{cyl}}(\theta, \varphi)$  may be in spherical coordinates by Eq. (C2). It is obvious that this equation is a one-dimensional non-smooth equation with a singularity at the line  $\theta = \theta_{\text{cyl,ed}}$ . The value of the singular azimuthal angle is

$$\theta_{\text{cyl,ed}} = \tan^{-1} \frac{a}{c}. \quad (19)$$

In our case, Eq. (19) acquires the value  $\theta_{\text{cyl,ed}} = \tan^{-1} 2 = 0.3524\pi$ .

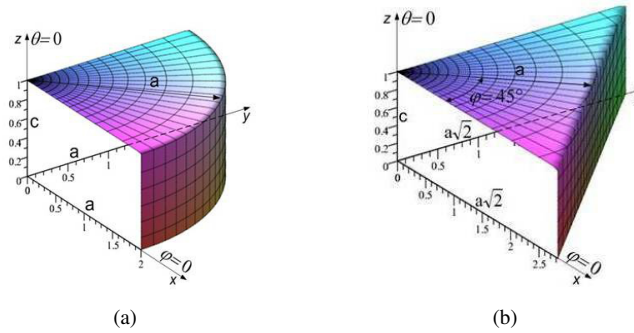


**Figure 3.** Simplest symmetric non-spherical shapes with  $c = 1$  and  $a = 2$ : (a) circular cylinder and (b) rectangular parallelepiped.

### 3.2 Reference models

Modeling of a circular cylinder by low-resolution spherical harmonics of the order  $L = 3$  is investigated. Generally, only symmetric part of the cylinder  $z > 0$  is considered. In spherical coordinates, the surface is interpreted as two-dimensional  $\theta$ - $\varphi$  subdomain, where a cylindrical surface is defined by Eq. (C2). A cylinder presents the axi-symmetric surface  $S_{R,cyl}(\varphi, \theta) \equiv S_{R,cyl}(\theta)$ , therefore, it is constant along the polar angle. On the other hand, spherical harmonics approximation has two-dimensional character, and local deviations are seen in SH model.

The illustration of numerically generated reference models, obtained by various strategies  $q$  with different discretization models  $k$ , is given in Fig. 4. Here, the section of cylinder defined by Eq. (C1) is drawn in  $Oxz$  Cartesian plane, where singularity in the intersection of edges is clearly observed. Nodes positions are characterised by coordinates  $x$  and  $z$ .

The refining strategy assumes that angular subdomain is covered with regular grid. Illustration of the first strategy ( $q = 1$ ) is given in Fig. 4a.

The second strategy ( $q = 2$ ) is regular equidistance refining strategy supported with four sequential schemes containing the data structure of previous sample is illustrated in Fig. 4b. It presumes regular equidistance subdivision of the cylinder section profile with constant cell size  $\Delta l = (a + c)/n_\varphi$  yielding, however, variable angular size  $\Delta\theta$ . Here, the sampling point matches exactly the singular intersection point.

The next strategy ( $q = 3$ ) is selected to illustrate a technique, where the global adaptive refining is combined with the local refinement. Presented sample (Fig. 4c) demonstrates the denser refining in the region near the singular point. The last strategy presents the Gauss points strategy ( $q = 4$ ), which is illustrated in Fig. 4d. This positioning presents actually regular logarithmic refinement at the boundaries of modelling domain disregarding internal singularity.

The reference threshold model denoted by thr is also considered as the most accurate numerical model, which was obtained by generation of a regular rectangular grid covering the angular  $\theta$ - $\varphi$ -plane. The threshold model is characterised by total number of  $N_{thr} = 16250$  of sampling points.

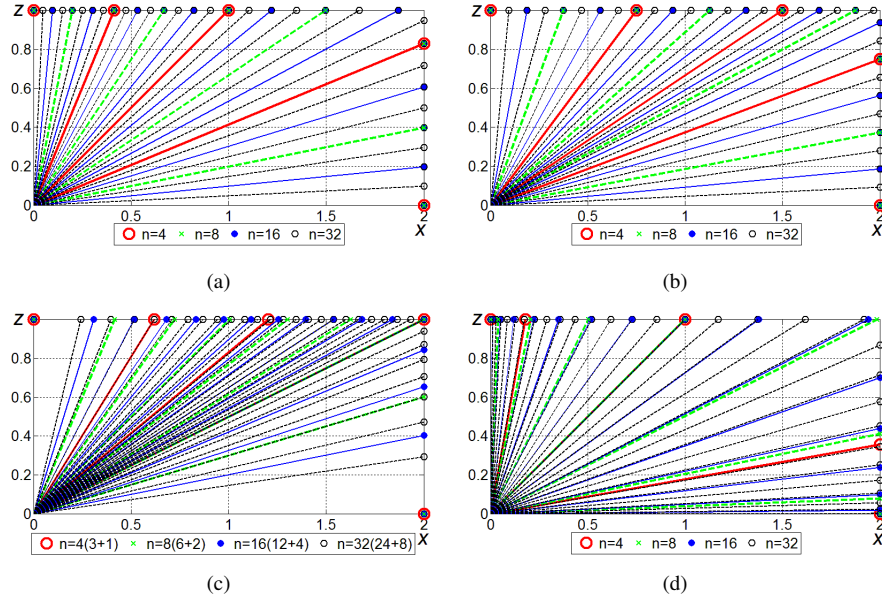


**Figure 4.** Illustration of reference models showing locations of sampling points for cylinder generated with different modelling discretization models  $k$  having radially varying number of cells  $n$  and various modelling strategies: (a) strategy  $q = 1$ , regular equiangular grid refinement; (b) strategy  $q = 2$ , regular equidistant grid refinement, (c) strategy  $q = 3$ , adaptive local grid refinement; (d) strategy  $q = 4$ , application of Gauss points.

The global quality is evaluated by Euclidian error norm. The choice of two local criteria is motivated below showing that the sign of the local deviation has some physical meaning leading to different particles properties.

### 3.3 Numerical results and discussion

A detailed comparison of all the above described  $qk$  reference models is shown in Table 1. The results, obtained by applying the threshold model, are also presented for the sake of comparison. Two types of descriptors, numerically calculated values and relative deviations, are listed in the table. The global quality of SH approximation is essentially evaluated by the normalized Euclidean norm  $\|D_{jqk}\|^2$  (column 5) obtained by Eq. (15). The relative deviations  $\delta_{LS,jqk}$  (column 6) are obtained with respect to the threshold error value  $\|D_{thr}\|^2 = 0.9539$ . Additionally, the values of average deviations  $\|D_{jqk}\|_{av} = \|D_{jqk}\|^2/N_{thr}$  (column 7) are given in order to evaluate the approximation magnitude. The most suitable values reflecting the minimal least-squares errors are marked with "\*".

Graphical information is also added in Fig. 5 to explain the numerical results. Here, cross-sectional profiles  $r(\theta)$ , numerically calculated at the polar angle  $\varphi = 0$ , are plotted. Exact analytically described profiles are also shown. The comparison of the best profiles, obtained by various strategies, is illustrated in Fig. 5a. Contribution of the grid refinements is illustrated in Fig. 5b, where four profiles, obtained by the adaptive grid

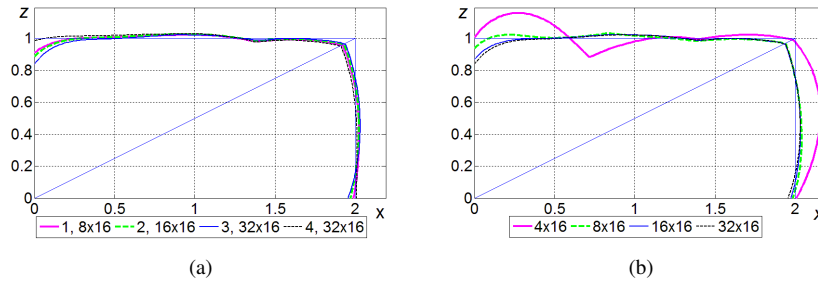


**Figure 5.** Illustration of SH approximation of cylinder, obtained by various strategies and different grids: (a) cross-sectional profiles corresponding to the minimal least square-errors norms obtained by different modelling strategies; (b) cross-sectional profiles obtained by the adaptive refinement strategy ( $q = 3$ ).

refinement strategy ( $q = 3$ ) with different numbers of positioning nodes listed in the legend, are shown.

On the basis of the values of the least-squares error norms, several observations could be manifested. It was found that the introduced locally adaptive refinement strategy ( $q = 3$ ) yields the minimal global deviations, characterised by quite a low error, about 2%. As to the other two schemes, the regular equidistance refinement ( $q = 2$ ), yielding a nearly logarithmic angular variation adaptive refinement of the grid in the vicinity of the corner, prevails over the equidistance refinement strategy ( $q = 1$ ). The Gauss point strategy ( $q = 4$ ) yields, however, very high errors in the range of 30%.

The global quality of approximation is also evaluated by calculating the surface area  $A$  and the body volume  $V$ . Thereby, the theoretical value of the surface area of cylinder  $A_{\text{cyl}}$  is obtained analytically according to Eq. (C4), while  $V_{\text{cyl}}$  according to Eq. (C3). The values of surface areas  $A_{jqk}$ , numerically calculated according to Eq. (17), are listed in column 10, while the volume values  $V_{jqk}$ , defined numerically by Eq. (18), are listed in column 12. The relative deviations  $\delta_{A,jqk} = |A_{\text{cyl}} - A_{jqk}|/A_{\text{cyl}}$  and  $\delta_{V,jqk} = |V_{\text{cyl}} - V_{jqk}|/V_{\text{cyl}}$  are evaluated by comparing both types of theoretical and numerical values. The results show that volumes are calculated with a very high accuracy and the error is below 0.01%. The accuracy of the surface area is lower. It has been found that, in the optimal case, the surface area is obtained with the accuracy 1.3%, which is better compared to the best least-squares estimation equal to 2.2%.

Instead of Eq. (16), two different, maximal and minimal, error norms were used to characterise the local approximation quality in the vicinity of specified regions.

The values of local descriptors (Table 1, columns 8–9) illustrate that it is difficult to find optimal refinement because a finer refinement of the grid not necessarily improves the approximation quality. The graphs in Fig. 5b demonstrate that the minimal error  $\delta_{LS}$ , obtained by the adaptive strategy, minimises the local errors in the vicinity of the singular corner, but increases deviation on the edges and especially on the symmetry planes. It is obvious that the choice of the best strategy is not straightforward, while the smallest error  $\delta_{LS} = 2.3\%$  was obtained with a denser grid. It could be noted that the minimal norm  $\|D_{3qk}\|_{\min} = 16.23\%$  (column 9 in Table 1) is much higher as compared to the minimal value that equals to 6.72%.

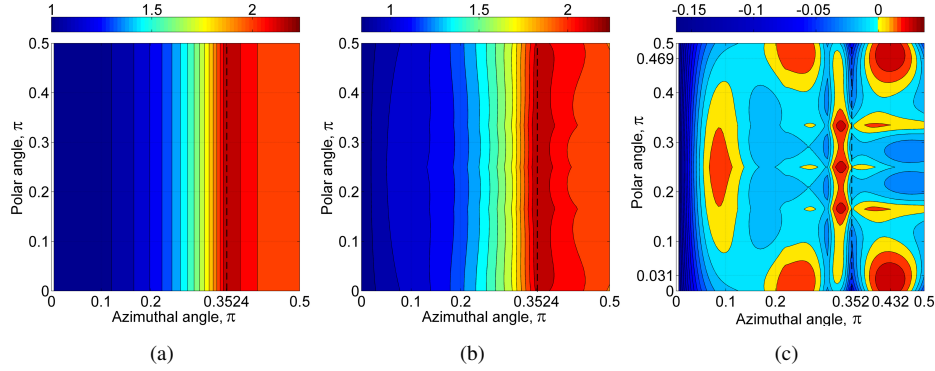


**Figure 6.** Two-dimensional illustration of SH model quality for cylinder – contour plots of the surface: (a) exact surface (Eq. (C2)); (b) SH approximation ( $L = 3$ ); (c) descriptor  $D_3$  ( $L = 3$ ).

To grasp the entire view, three-dimensional images of the particle surface  $S_R(\theta, \varphi)$  are presented graphically in Fig. 6. Here, contour plots of the particle surface  $S_R(\theta, \varphi)$  over two-dimensional angular  $\theta\varphi$ -domain are shown. The exact surface, obtained by Eq. (C2), is shown in Fig. 6a, the SH approximation, obtained by the strategy  $q = 3$ , is shown in Fig. 6b. Exact surface is characterised by parallel lines. Approximated surface indicates the local deviations in polar directions. Quantitatively, the values of radius at boundaries are equal to cylinder sizes  $c = 1$  and  $a = 2$ , while the maximal value  $\sqrt{5} = 2.24$  indicates location of the sharp edge  $\theta_{\text{cy},\text{ed}} = 0.3524\pi$  obtained according to Eq. (19). Axial symmetry is reflected by constant angular variation  $S_R(\varphi) = \text{const}$  along the entire sector  $0 \leq \varphi \leq \pi/2$ . Small, visually hardly detectable deviations of these lines on  $\varphi = 0$  in Fig. 6b indicate numerical errors.

Detailed map of deviations corresponding to the definition of descriptor (14) is presented in Fig. 6c. It was found that deviations shown in figure have different consequences for the future DEM applications. The first effect is related to the external deviations of particle surface characterised by their positive values. They are of major importance in particles analysis, since they indicate artificial increase of the effective particle volume. This yields undesirable effects in particle packing problems. The highest value of the deviations (Fig. 6c) on the cylinder end-section ( $\theta \leq \theta_{\text{ed}}$ ) could be interpreted as artificial increase of cylinder height yielding  $\Delta c = 0.0209$ . Thus, this deviation yields an increase of cylinder volume  $\Delta V_1 = 2\%$ . The highest values of the cylinder lateral side is  $\Delta a = 0.0366$  yielding the increase of volume  $\Delta V_2 = 3\%$ . This sample shows that artificial increase by 5% could be expected.

The other two effects are related to internal, or negative, deviations, which are characterised by the minimum error norm  $\|D_{3qk}\|_{\min}$ . The negative deviations observed near the symmetry axes of the cylinder are related to the loss of convexity of the surface as a whole. This type of local deviations will have negligible effect for particles contact. The third effect is attributed to the larger internal deviations detected in the vicinity of the sharp edges or corners. This effect has positive consequences since concentration of stresses in the contact of sharp corners may be diminished.

**Table 1.** Results of SH description of the shapes by  $L = 3$  order expansion – values of various descriptors.

q	2	3	4	5	6	7	8	9	10	11	12	13
Strat- tegy	Refer. k	Grid $n_\theta \times n_\varphi$	Points number $N_k$	LS error $\ D_{jgk}\ ^2$	$\delta_{LS}$	Average deviation $\ D_{jgk}\ _{av}$	Max. (ext.) error $\ D_{jgk}\ _{max}$	Min. (int.) error $\ D_{jgk}\ _{min}$	Surface area $A_{jgk}$	$\delta_A$	$V_{jgk}$	Volume $\delta_V$
Circular cylinder												
1	3	$16 \times 16$	273	1.1076	0.1611	0.0000682	0.0382*	-0.0942	49.207	0.0210	25.087	0.0018
	4	$32 \times 16$	545	1.1410	0.1961	0.0000702	0.0391	-0.0951	49.247	0.0203	25.100	0.0013
2	3	$16 \times 16$	273	1.0005*	0.0488*	0.0000616	0.0371*	-0.1128	49.389	0.0174	25.110	0.0009
	4	$32 \times 16$	545	1.0083	0.0570	0.0000621	0.0385	-0.0851	49.408*	0.0170*	25.119*	0.0005*
3	1	$4 \times 16$	69	4.4318	3.6460	0.0002727	0.2313	-0.1582	53.705	0.0684	27.506	0.0944
	2	$8 \times 16$	137	1.1247	0.1790	0.0000692	0.0488	-0.0672**	50.020**	0.0049**	25.233	0.0039
	3	$16 \times 16$	273	0.9855	0.0331	0.0000606	0.0397	-0.1304	49.590	0.0134	25.158	0.0009
	4	$32 \times 16$	545	0.9755**	0.0226**	0.0000600	0.0377*	-0.1623	49.595	0.0133	25.132**	0.00004*
4	4	$32 \times 16$	545	1.2483*	0.3086*	0.0000768	0.04*	-0.1022	49.138	0.0224	25.108*	0.0010*
Threshold model			16250	0.9539		0.0000587		Analytical	50.265		25.133	
Rectangular parallelepiped												
5	5	$8 \times 8$	73	5.0326*	0.0794*	0.0003071	0.1812	-0.3657*	60.613*	0.0529*	31.845*	0.0048*
	3	$16 \times 16$	273	5.0638	0.0861	0.0003090	0.1659	-0.3819	60.316	0.0577	31.725	0.0086
	8	$32 \times 32$	1057	5.1169	0.0975	0.0003123	0.155	-0.3914	60.114	0.0607	31.704	0.0093
6	5	$8 \times 8$	73	5.0326	0.0794	0.0003071	0.2144	-0.3318	61.688*	0.0361*	32.251	0.0078
	3	$16 \times 16$	273	4.8182	0.0335	0.0002940	0.2277	-0.3357	61.194	0.0438	31.898*	0.0032*
	8	$32 \times 32$	1057	4.7566**	0.0202**	0.0002903	0.2244	-0.3256*	61.505	0.0390	31.874	0.0039
7	8	$32 \times 32$	1057	5.0086	0.0743	0.0003057	0.1464	-0.3583	61.223*	0.0434*	31.797	0.0063
8	8	$32 \times 32$	1057	4.9478	0.0613	0.0003020	0.2129	-0.4257	62.485**	0.0237**	31.657	0.0107
Threshold model			16380	4.6622		0.0000285		Analytical	64.00		32.00	

## 4 SH modelling of the rectangular parallelepiped

### 4.1 Modelling approach

The second shape, a rectangular parallelepiped (Fig. 3b), presents a large group of polyhedral shapes [2, 16]. A parallelepiped presents a complex shape within three pairs of mutually parallel planes intersections resulting in sharp edges and vortexes. To reduce computational expenses, the sharp edges may be smoothed, and polyhedral shapes are replaced with spheropolyhedra [8, 16].

A rectangular parallelepiped is considered similarly as previously described cylinder. The global shape is characterised by two sizes  $a$  and  $c$ . The surface is centered on the origin. Considering spherical coordinates, the reference polar angle  $\varphi = 0$  is oriented along the face diagonal. Consequently, the parallelepiped occupies the subspace between angles  $0 \leq \varphi \leq \pi/2$ . Finally, the surface of the parallelepiped  $S_{R,\text{par}}(\varphi, \theta)$  is described by non-smooth Eq. (P2). Concerning azimuthal variation, the angular domain is divided into two regions by the sharp edge  $\theta_{\text{par,ed}}(\varphi)$ . The edge is parallel to the plane  $Oxy$  and is described as follows:

$$\theta_{\text{par,ed}}(\varphi) = \frac{\tan^{-1}(\sqrt{2}a/c)}{\cos \varphi}. \quad (20)$$

The volume and the surface area are defined by Eq. (P3) and Eq. (P4).

Contrary to the cylinder, rotational symmetry is not held, and the two-dimensional discretization of the angular subdomain in both angular directions is required. Two strategies of the azimuthal refinement, assuming equiangular (strategy  $q = 2$ ) and adaptive ( $q = 3$ ) refinements of the grid structure and yielding the minimal approximation error, are used for further investigation. The illustration of the polar refinement is given in Fig. 7. Here, the equiangular polar refinement (Fig. 7a) characterised by a constant cell size  $\Delta\varphi$  and the adaptive polar refinement (Fig. 7b) combined with the adaptive azimuthal refinement are shown. The equidistance rectangular threshold model (Fig. 7c) with the total number  $N_{\text{thr}} = 16380$  of points is generated in order to avoid the coincidence of positioning points. The points of the threshold model are explored further in the characterisation of the actual model  $A_{jqk}$ .

Combination of the polar and azimuthal refinement allows constructing four new two-dimensional strategies. To avoid confusion with previous notations, increased indexes for

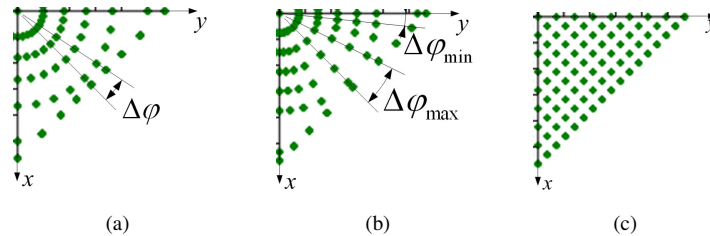


**Figure 7.** Positioning of the sampling points on the face of a parallelepiped used in different modelling strategies: (a) equiangular polar refinement strategy; (b) adaptive polar refinement strategy; (c) threshold refinement.

new strategies denoted further as  $q = 5, 6, 7, 8$  were applied, i.e. strategy  $q = 5$  means combination of the equiangular polar and the equiangular azimuthal refinement, strategy  $q = 6$  means combination of the adaptive azimuthal refinement with equiangular polar refinement, etc.

## 4.2 Numerical results and discussion

Numerical testing is aimed to find the best approximation by considering low-resolution spherical harmonics of order  $L = 3$ . In total,  $q \times k = 20$  reference models, comprising five discrete grids with ( $k = 3, 5, \dots, 8$ ), i.e.  $8 \times 8$ ,  $12 \times 12$ ,  $16 \times 16$ ,  $24 \times 24$  and  $32 \times 32$ , sets of sampling points generated by the strategies ( $q = 5, \dots, 8$ ) were examined.

A detailed comparison of all the above described  $qk$  reference models is illustrated in Table 1. The results, obtained by applying the threshold model, are also presented for comparison. The relative deviations  $\delta_{LS}$  (column 6) are obtained with respect to the threshold error value  $\|D_{\text{thr}}\|^2 = 4.6622$ .

The global quality of approximation is also evaluated by calculating the surface area  $A$  and the body volume  $V$  of parallelepiped. Thus, the theoretical value of the surface area  $A_{\text{par}}$  is obtained analytically according to Eq. (P4), while  $V_{\text{par}}$  – according to Eq. (P3). The values of the surface area  $A_{jqk}$ , numerically calculated according to Eq. (17), are listed in column 10, while the volume values  $V_{jqk}$ , defined numerically by Eq. (18), are listed in column 12. The relative deviations  $\delta_{A,jqk} = |A_{\text{par}} - A_{jqk}|/A_{\text{par}}$  and  $\delta_{V,jqk} = |V_{\text{par}} - V_{jqk}|/V_{\text{par}}$  are evaluated by comparing both types of theoretical and numerical values. The results show that volumes are calculated with a very high accuracy of less than 1%. The accuracy of the surface area is in the range between 3–5%. Both of them are smaller as compared to the least-squares error. Cross-sectional profiles in terms of  $r(\theta)$  curves plotted at the polar angle  $\varphi = 0$  and  $\varphi = \pi/4$  are presented graphically in Fig. 8.

To grasp the entire view, the three-dimensional images of the particle surface  $S_R(\theta, \varphi)$  are presented graphically in Fig. 9 as contour plots over the two-dimensional angular  $\theta\varphi$ -domain. Here, the exact surface is shown in Fig. 9a, the SH model, obtained by the strategy  $q = 6$ , is shown in Fig. 9b. A detailed map of deviations, corresponding to definition of the descriptor Eq. (14), is presented in Fig. 9c.

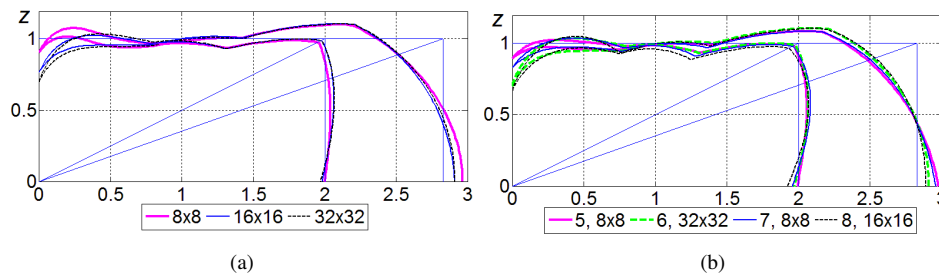


**Figure 8.** Illustration of parallelepiped approximation by using SH: (a) cross-sectional profiles obtained by  $L = 3$  expansion degree SH using the strategy  $q = 6$  for different refinements; (b) profiles corresponding to the best reference models.

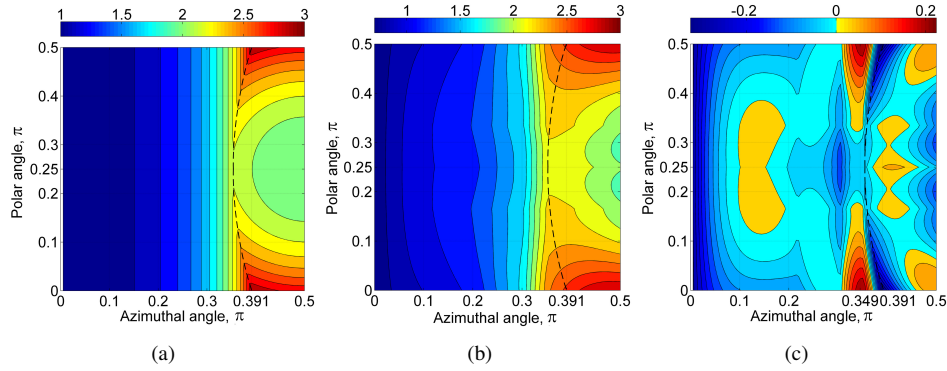


**Figure 9.** Two-dimensional illustration of the SH model quality for a parallelepiped – contour plots of the surface: (a) exact analytical surface; (b) SH approximation by degree  $L = 3$ ; (c) the descriptor  $D$ .

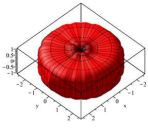
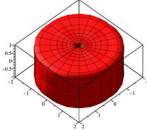
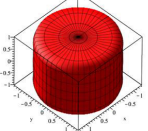
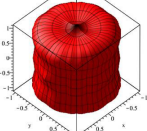
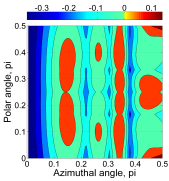
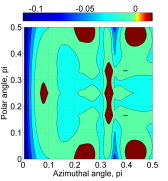
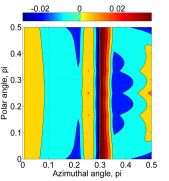
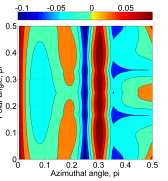
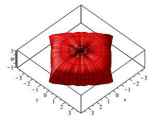
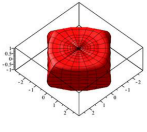
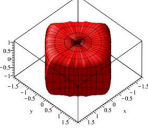
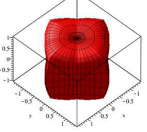
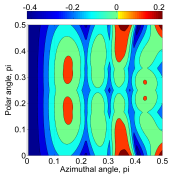
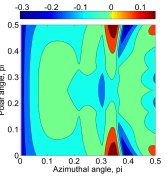
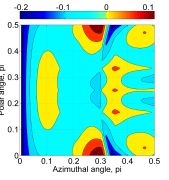
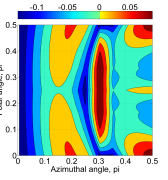
## 5 Comparison study of low-resolution harmonics for various shapes

In the previous sections, characteristic features of the SH models were demonstrated by exploring a cylinder and parallelepiped. They were limited, however, to a single set of two-size parameters, the length  $c = 1$  and cross-sectional size, or thickness,  $a = 2$ . In order to compare various values of  $a$  and  $c$ , all shapes are described in terms of a dimensional size parameter  $R$  and non-dimensional factors  $\bar{a} = a/R$  and  $\bar{c} = c/R$ , respectively (see [1]). If the parameter  $c$  is considered as a length parameter and perpendicular sizes  $b = a$  as cross-sectional perpendicular parameters, the ratio  $c/a$  means the elongation degree  $k_{\text{elon}} = c/a$ . In the symmetric section, this quantity is also a flatness degree [1].

The approximated particle shape was characterized by a set of  $M = 16$  coefficients, corresponding to the expansion degree  $L = 3$ . Suitability of lower-resolution harmonics to description of particles was examined by considering the flattening of initially selected shapes for specified values of the elongation degree  $k_{\text{elon}} = 1, 0.75, 0.5, 0.4$ . The earlier results, obtained for the cylinder and parallelepiped with the elongation  $k_{\text{elon}} = 0.5$ , are used as a template for further investigations.

The pictorial summary of models of all shapes is shown in Table 2. Three-dimensional views show that the approximated models retain the basic features of original shapes, while local deviations near the axis are observed. Additionally, sharp edges are transformed into locally smooth surfaces. The local variations of the surface are better illustrated by contour plots. The shapes are qualitatively characterised by different error indicators. The best accuracy is achieved in the approximation of particle volumes, while the accuracy of surface area correlates with the least-squares error. It could be stated that generally the cylinder is approximated by spherical harmonics with a higher accuracy yielding average errors of 2%. The parallelepiped is approximated with the error in the range of 5%. Scattering of the results could be explained by the shape of spherical harmonics involved, i.e. each particular figure is approximated by different harmonics, and no

**Table 2.** Pictorial summary of different shapes: three-dimensional views, contour plots of surface deviation, defined by Eq. (14), and relative errors.

	0.4	0.5	0.75	1
Cylinder				
				
				
	$\delta_A = 2.11\%$ $\delta_V = 1.02\%$ $\delta_{LS} = 1.70\%$	$\delta_S = 1.43\%$ $\delta_V = 0.06\%$ $\delta_{LS} = 2.26\%$	$\delta_S = 0.56\%$ $\delta_V = 0.52\%$ $\delta_{LS} = 0.69\%$	$\delta_S = 1.29\%$ $\delta_V = 1.08\%$ $\delta_{LS} = 1.51\%$
Parallelepiped				
				
				
	$\delta_S = 1.86\%$ $\delta_V = 0.79\%$ $\delta_{LS} = 6.72\%$	$\delta_S = 4.53\%$ $\delta_V = 0.32\%$ $\delta_{LS} = 2.02\%$	$\delta_S = 3.20\%$ $\delta_V = 1.13\%$ $\delta_{LS} = 4.49\%$	$\delta_S = 1.99\%$ $\delta_V = 0.51\%$ $\delta_{LS} = 5.08\%$

regularity is detected. Since the results were obtained by a limited number of positioning, a higher accuracy could be achieved by a detailed optimization analysis.

## 6 Concluding remarks

Comprehensive modelling study, presented in this paper, was performed considering the application of the low-resolution spherical harmonics (SH) limited by the expansion degree  $L = 3$ . The quality of approximation was evaluated by global descriptors such as the least-squares norm, the particle surface area, and the volume. It has been found, however,

that the low-resolution harmonics are very sensitive to the positions of sampling points, and the approximation quality increases by applying locally adaptive positioning.

Concerning particular shapes, the cylindrical shapes are approximated with the 2% error. Due to the presence of sharp edges and vertices, the parallelepiped is approximated with a lower accuracy characterised by the average 5% error. The scattering of results could be explained by the different harmonics having different contributions for specified shapes.

The presented results discovered that low-resolution spherical harmonics yield a satisfactory quality for description of quite complicated shapes with sharp edges. Therefore, they may be further implemented in the simulation of particulate materials.

## Appendix

**Table A.1.** Low resolution spherical harmonics normalized by factor  $1/2\sqrt{\pi}$ .

Expansion order	Expansion degree		
	$L = 0$	$L = 1$	$L = 3$
$m = -3$			$(\sqrt{70}/4) \sin^3\theta\sin 3\varphi $
$m = -2$			$(\sqrt{105}/2) \cos\theta\sin^2\theta\sin 2\varphi $
$m = -1$		$\sqrt{3} \sin\theta\sin\varphi $	$(\sqrt{42}/4) \sin\theta(5\cos^2\theta - 1)\sin\varphi $
$m = 0$	1	$\sqrt{3} \cos\theta $	$(\sqrt{7}/2) \cos\theta(5\cos^2\theta - 3) $
$m = 1$		$\sqrt{3} \sin\theta\cos\varphi $	$(\sqrt{42}/4) \sin\theta(5\cos^2\theta - 1)\cos\varphi $
$m = 2$			$(\sqrt{105}/2) \cos\theta\sin^2\theta\cos 2\varphi $
$m = 3$			$(\sqrt{70}/4) \sin^3\theta\cos 3\varphi $

**Table A.2.** Summary of analytical descriptors of particles shapes.

Cylinder	
$S(x, y, z)$	$\begin{cases} x^2 + y^2 & \text{for } -c < z < c, \\ z \pm c & \text{otherwise} \end{cases} \quad (\text{C1})$
$S_R(\varphi, \theta)$	$\begin{cases} c/\cos\theta & \text{for } 0 \leq \theta \leq \theta_{\text{ed}}, \\ a/\sin\theta & \text{for } \theta_{\text{ed}} \leq \theta \leq \pi/2 \end{cases} \quad (\text{C2})$
$V$	$\pi a^2 c \quad (\text{C3})$
$S$	$2\pi a(a + c) \quad (\text{C4})$
Parallelepiped	
$S(x, y, z)$	$\begin{cases} x \pm a & \text{for } -a \leq y \leq a, -c \leq z \leq c, \\ y \pm a & \text{for } -a \leq x \leq a, -c \leq z \leq c, \\ z \pm c & \text{for } -a \leq x \leq a, -a \leq y \leq a \end{cases} \quad (\text{P1})$
$S_R(\varphi, \theta)$	$\begin{cases} c/\cos\theta & \text{for } \varphi \leq \pi/4, 0 \leq \theta \leq \tan^{-1}(a/c\cos\varphi), \\ a/\sin\theta\cos\varphi & \text{for } \varphi \leq \pi/4, \tan^{-1}(a/c\cos\varphi) \leq \theta \leq \pi/2, \\ c/\cos\theta & \text{for } \varphi > \pi/4, 0 \leq \theta \leq \tan^{-1}(a/c\sin\varphi), \\ a/\sin\theta\sin\varphi & \text{for } \varphi > \pi/4, \tan^{-1}(a/c\sin\varphi) \leq \theta \leq \pi/2 \end{cases} \quad (\text{P2})$
$V$	$a^2 c \quad (\text{P3})$
$S$	$4ac + 2a^2 \quad (\text{P4})$

## References

1. S.J. Blott, K. Pye, Particle shape: A review and new methods of characterization and classification, *Sedimentology*, **55**:31–63, 2008.
2. C.W. Boon, G.T. Houlsby, S. Utili, A new algorithm for contact detection between convex polygonal and polyhedral particles in the discrete element method, *Comput. Geotech.*, **44**:73–82, 2012.
3. J.W. Bullard, E.J. Garboczi, Defining shape measures for 3D star-shaped particles: Sphericity, roundness and dimensions, *Powder Technol.*, **249**:241–252, 2013.
4. P. Courrieu, Fast computation of Moore–Penrose inverse matrices, *Neural Information Processing – Letters and Reviews*, **8**(2):25–29, 2005.
5. P.A. Cundall, O.D.L. Strack, A discrete numerical model for granular assemblies, *Geotechnique*, **29**:47–65, 1979.
6. A. Džiugys, B. Peters, An approach to simulate the motion of spherical and non-spherical fuel particles in combustion chambers, *Granul. Matter*, **3**(4):231–265, 2001.
7. J. Feinauer, A. Spetl, I. Manke, S. Strege, A. Kwade, A. Pott, V. Schmidt, Structural characterization of particle systems using spherical harmonics, *Mater. Charact.*, **106**:123–133, 2015.
8. S.A. Galindo-Torres, D.M. Pedroso, Molecular dynamics simulations of complex-shaped particles using Voronoi-based spheropolyhedra, *Phys. Rev. E*, **81**:061303, 2010.
9. E.J. Garboczi, Three-dimensional mathematical analysis of particle shape using X-ray tomography and spherical harmonics: Application to aggregates used in concrete, *Cement Concrete Res.*, **32**(10):1621–1638, 2002.
10. E.J. Garboczi, Three dimensional shape analysis of JSC-1A simulated lunar regolith particles, *Powder Technol.*, **207**(1-3):96–103, 2011.
11. E.J. Garboczi, J.W. Bullard, Contact function, uniform-thickness shell volume, and convexity measure for 3D star-shaped random particles, *Powder Technol.*, **237**:191–201, 2013.
12. M. Grigoriu, E. Garboczi, C. Kafali, Spherical harmonic-based random fields for aggregates used in concrete, *Powder Technol.*, **166**(3):123–138, 2006.
13. M. Kodam, R. Bharadwaj, J. Curtis, B. Hancock, C. Wassgren, Cylindrical object contact detection for use in discrete element method simulations. Part I – Contact detection algorithms, *Chem. Eng. Sci.*, **65**(22):5852–5862, 2010.
14. J.P. Latham, A. Munjiza, The modelling of particle systems with real shapes, *Philos. Trans. R. Soc. Lond., Ser. A, Math. Phys. Eng. Sci.*, **362**(1822):1953–1972, 2004.
15. X. Liu, E.J. Garboczi, M. Grigoriu, Y. Lu, S.T. Erdogan, Spherical harmonic-based random fields based on real particle 3D data: Improved numerical algorithm and quantitative comparison to real particles, *Powder Technol.*, **207**(1-3):78–86, 2011.
16. G. Lu, J.R. Third, C.R. Muller, Discrete element models for non-spherical particle systems: From theoretical developments to applications, *Chem. Eng. Sci.*, **127**:425–465, 2015.
17. M.-H. Mouse, R. Chaine, S. Akkouche, E. Galin, Toward an efficient triangle-based spherical harmonics representation of 3D objects, *Comput. Aided Geom. Des.*, **25**(8):561–575, 2008.
18. B. Zhou, J. Wang, B. Zhao, Micromorphology characterization and reconstruction of sand particles using micro X-ray tomography and spherical harmonics, *Eng. Geol.*, **184**:126–137, 2015.